

# On the identification of substructure in phase-space using orbital frequencies

Facundo A. Gómez<sup>\*</sup> & Amina Helmi

*Kapteyn Astronomical Institute, University of Groningen, P.O. Box 800, 9700 AV Groningen, The Netherlands*

## ABSTRACT

We study the evolution of satellite debris to establish the most suitable space to identify past merger events. We find that the space of orbital frequencies is very promising in this respect. In frequency space individual streams can be easily identified, and their separation provides a direct measurement of the time of accretion. We are able to show for a few idealised gravitational potentials that these features are preserved also in systems that have evolved strongly in time. Furthermore, this time evolution is imprinted in the distribution of streams in frequency space. We have also tested the power of the orbital frequencies in a fully self-consistent (live) N-body simulation of the merger between a disk galaxy and a massive satellite. Even in this case streams can be easily identified and the time of accretion of the satellite can be accurately estimated.

**Key words:** galaxies: formation – galaxies: kinematics and dynamics – methods: analytical – methods: N-body simulations

## 1 INTRODUCTION

In the current standard cosmological model, known as  $\Lambda$ CDM, galaxies like our own Milky Way are formed bottom-up, through the merger and accretion of smaller building blocks that come together due to their gravitational attraction (e.g. White & Rees 1978).

This model is being continuously tested and many questions and puzzles remain to be addressed. An example is the large number of bound substructures predicted to orbit galaxies like the Milky Way and M31 compared to the observed abundance of satellite galaxies in these systems (Klypin et al. 1999; Moore et al. 1999), although several solutions have been proposed (e.g. Bullock et al. 2000). The formation of realistic disk galaxies in full cosmological simulations remains another great challenge (e.g. Steinmetz & Navarro 1999) yet steady progress is being made (e.g. Governato et al. 2004, 2007; Scannapieco et al. 2009).

One strong test of the current paradigm may be performed through observations of the stellar halos of galaxies like the Milky Way. For example, if the Galaxy was formed in a hierarchical fashion via mergers, then we should be able to find fossil signatures of these events in the present day phase-space distribution of halo stars. This idea was strongly exalted after the discovery of the disrupting Sgr dwarf galaxy by Ibata et al. (1994). In the following years further debris from accretion events was discovered, not only in the halo

(Helmi et al. 1999; Grillmair 2006; Belokurov et al. 2006) but also in the disk of our Galaxy (Eggen 1996; Ibata et al. 2003; Yanny et al. 2003; Navarro, Helmi & Freeman 2004; Helmi et al. 2006).

However, if the hierarchical scenario is correct, we are still far from having unveiled every single stream associated to each merger event the Galaxy has experienced in its lifetime. Helmi, White & Springel (2003) by combining numerical simulations with analytic work predicted that there should be several hundreds of cold stellar streams present in the vicinity of the Sun (see also Vogelsberger et al. 2008). The short dynamical time scales, especially in the Solar neighbourhood, are the basic reason behind why such a large number is expected. An accreted satellite, orbiting in the inner regions of the Galaxy will give rise to multiple stellar streams in a relatively short period of time. As shown by Helmi & White (1999) the spatial density of these streams is a strongly decreasing function of time. Consequently, substructure associated to a past accretion event is expected to have a very low-density contrast, making its detection very difficult from its distribution in space. On the other hand, due to the conservation of phase-space density, the velocity dispersion of a stream will decrease as time goes by, making the streams tighter in the velocity domain.

The arguments above highlight the need for full 6D phase-space information to completely disentangle the predicted wealth of substructure. Furthermore, samples of at least 1,000 halo stars would appear to be necessary for this enterprise. Statistical arguments using the revised NLTT (New Luyten Two Tenths, Gould & Salim 2003;

<sup>\*</sup> Email: gomez@astro.rug.nl

Salim & Gould 2003) proper motion survey have been used to measure the amount of granularity (associated to moving groups) in the stellar halo near Sun. Gould (2003) has shown that no streams are present in this region of the Galaxy that contain more than approximately 5% of the halo stars near the Sun. This estimate is in good agreement with the expectations described above, but does not provide a direct confirmation of the predictions. Spectroscopic surveys such as RAVE (Zwitter et al. 2008) and SEGUE (Klement, Fuchs & Rix 2008, Smith et al. in preparation) should be helpful in identifying further nearby streams, if present, but the breakthrough will take place only with the astrometric satellite *Gaia* (Perryman et al. 2001). *Gaia*, expected to be launched in 2011, will measure the positions and motions of  $10^9$  stars with very high accuracy.

Given the datasets that soon will become available it is natural to ask what is the optimal way to discover merger debris. More precisely, the question we would like to address in this work is what is the best space to look for substructure if our goal is to disentangle how the Galaxy was assembled.

The first steps in this direction have been presented by Helmi & de Zeeuw (2000). These authors analysed simulations of the disruption of satellite galaxies in a fixed Galactic potential and concluded that the “integrals-of-motion” space defined by the energy, the total angular momentum and its  $z$ -component ( $E, L, L_z$ ) is very suitable for identifying the remains of past accretion events. Even in fully self-consistent cosmological simulations, disrupted satellites still appear as coherent structures in this “integrals of motion” space (Knebe et al. 2005). Font et al. (2006) demonstrated the power of complementary chemical abundance information to disentangle debris from different events. Arifyanto & Fuchs (2006) have used for samples of nearby stars the space defined by  $(U^2 + 2V^2)^{1/2}$  and  $V$ , where  $U$  is the radial velocity in the Galactic plane, and  $V$  is the velocity component in the direction of rotation. More recently McMillan & Binney (2008) proposed that action-angle coordinates, and in particular, the orbital frequencies could conform a very convenient set of variables to identify nearby substructure.

In this paper we explore further the power of the orbital frequencies. We start our journey by briefly reviewing the concept of action-angle variables in Section 2. In Section 3 we discuss in depth the space of orbital frequencies. We characterise the distribution of debris in a few simple cases and in particular, in a static spherical potential. In Section 4 we analyse how the structure of this space is altered in a time dependent (still rigid) potential. Finally, in Section 5 we focus on a live N-body simulation of the accretion of a massive satellite onto a pre-existing thin disk. We discuss and summarise our results in Section 6.

## 2 THE ACTION-ANGLE VARIABLES

Let us consider a dynamical system with a time-independent Hamiltonian  $H(\mathbf{p}, \mathbf{q})$ , where  $(\mathbf{p}, \mathbf{q})$  is a set of  $2n$  canonical coordinates. The dynamical state of this system is governed by the Hamilton’s equations

$$\dot{p}_i = -\frac{\partial H}{\partial q_i}, \quad \dot{q}_i = \frac{\partial H}{\partial p_i}, \quad (1)$$

with  $i = 1, \dots, n$ .

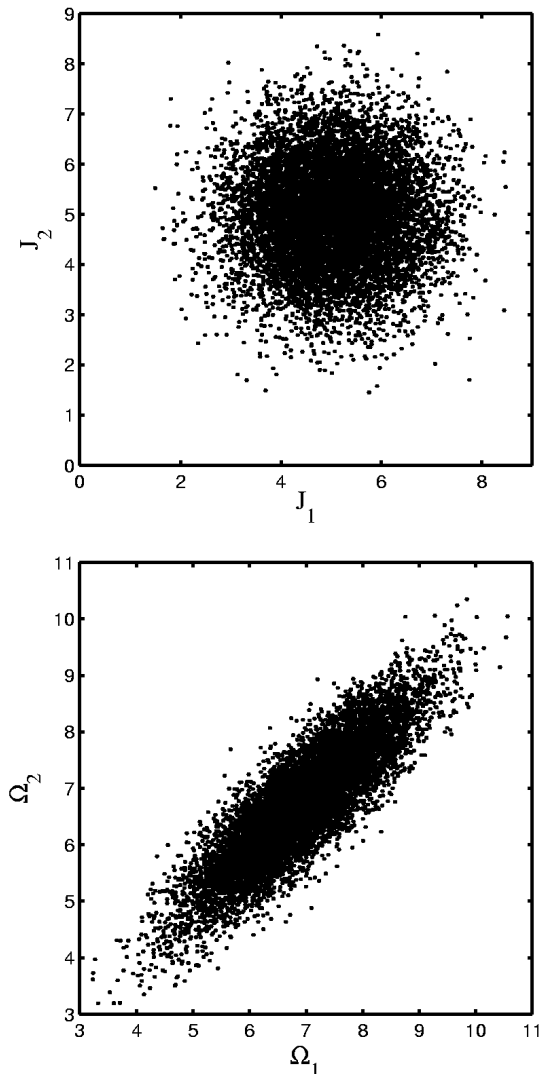


**Figure 1.** Distribution of all particles in the satellite in actions (upper panel) and frequency (lower panel) space.

The evolution of a system may be expressed much more simply by performing a canonical transformation of coordinates such that the equations of motion are

$$\dot{P}_i = -\frac{\partial H(\mathbf{P})}{\partial Q_i} = 0, \quad \dot{Q}_i = \frac{\partial H(\mathbf{P})}{\partial P_i} = \Omega_i(\mathbf{P}), \quad (2)$$

with solutions

$$Q_i = Q_i^0 + \Omega_i t, \quad P_i = P_i^0. \quad (3)$$

If the system under study is such that the motion is periodic, then this set of canonical variables is known as action-angle variables.

In a spherical potential  $\Phi(r)$ , the radial action is

$$J_r = \frac{1}{\pi} \int_{r_1}^{r_2} dr \frac{1}{r} \sqrt{2[E - \Phi(r)]r^2 - L^2} \quad (4)$$

where  $L$  is the total angular momentum,  $r_1$  and  $r_2$  the turning points in the radial direction and

$$J_\phi = L_z, \quad J_\theta = L - L_z \quad (5)$$

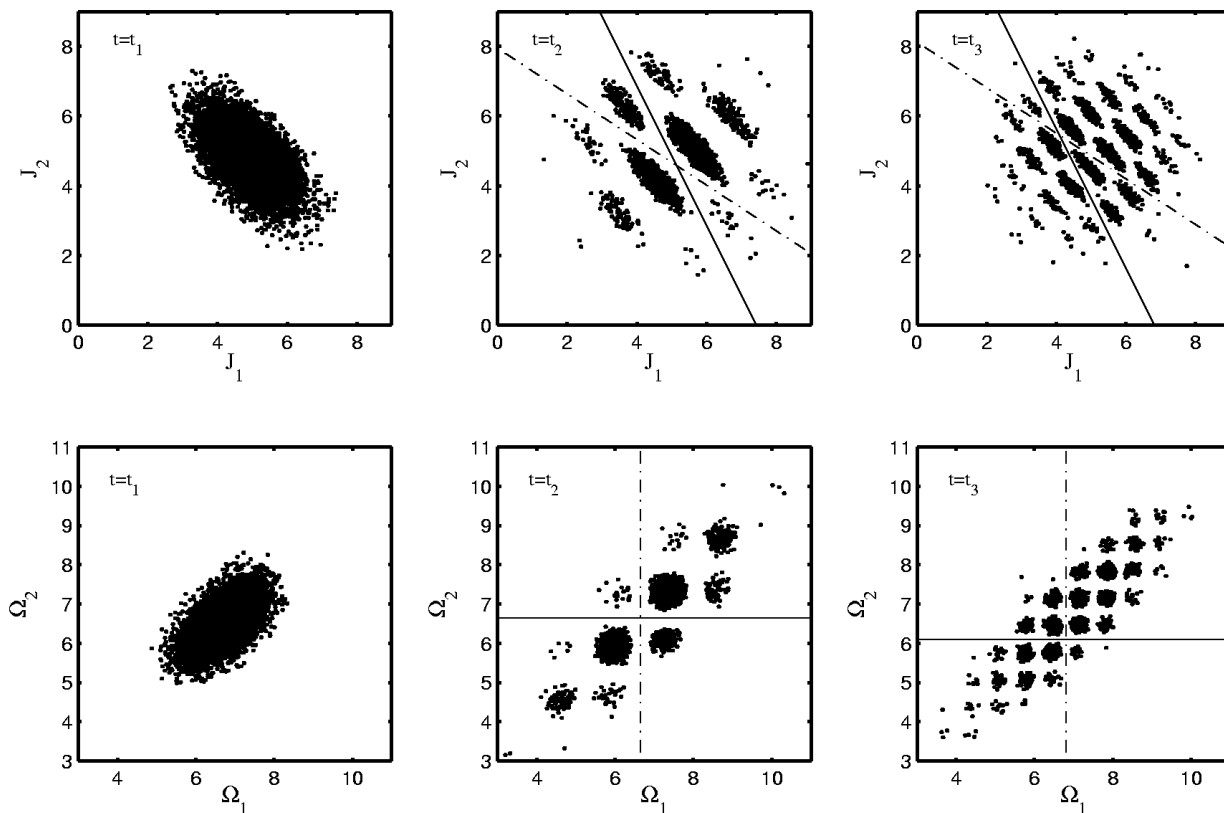


**Figure 2.** Distribution of particles in actions (upper panels) and frequency (lower panels) space located in a small region of the angle space at three different times. Each clump represents a particular stream crossing this region at the time considered. The solid lines indicate  $\Omega_2 = cst$  whereas the dotted-dashed lines represent lines of constant  $\Omega_1$ , as shown in the bottom panels.

are the angular actions. The frequencies of motion  $\Omega_i = \partial H / \partial J_i$ , can be derived by differentiation of the implicit function

$$g = J_r - \frac{1}{\pi} \int_{r_1}^{r_2} dr \frac{1}{r} \sqrt{2[E - \Phi(r)]r^2 - L^2} \quad (6)$$

defined by Eq. (4). For more details, see e.g., Goldstein, Poole & Safko (2001).

### 3 FREQUENCY SPACE FOR STATIC POTENTIALS

#### 3.1 Toy-Model

In order to become familiar with the space of orbital frequencies, we first develop a simple toy-model and follow the evolution of a satellite in this space.

Let us consider a satellite (i.e. a system of particles that are initially strongly clustered in phase-space) orbiting under the influence of an arbitrary gravitational potential. For simplicity, we consider a system with only two independent frequencies of motion. We will also assume that the initial distribution in action-angle space of the satellite follows a multivariate Gaussian (with no correlation among the different directions) as shown in Figure 1. In this space, the location of a given particle will vary only due to the evolution of the angle coordinates. The rate of evolution, i.e.

the frequencies, is completely determined by the underlying potential in which our satellite evolves (see Eq. (3)). The other two coordinates, i.e., the actions, will remain constant in time.

Here we shall assume that we can express the frequencies in the following way:

$$\Omega_1 = c_1 J_1 + c_2 J_2, \quad (7)$$

$$\Omega_2 = c_3 J_1 + c_4 J_2,$$

where  $c_i$  are constants. In general, the relation between the frequencies and the actions is more complex, and depends on the specific form of the gravitational potential.

Typically, we have access to samples of stars located in a particular region of space such as, for example, the Solar neighbourhood. This constraint acts as a filter, implying that we only observe the subset of stars with orbital properties such that they are in this particular location at the time of observation. To mimic this, we focus on the particles located in a small region of the angles' space in our toy-model. Figure 2 shows the distribution of these particles in the space of actions and of frequencies at three different times ( $0 < t_1 < t_2 < t_3$ ).

As discussed by McMillan & Binney (2008) the particles passing through a particular location of (angle-)space are distributed in different patches or streams. With time, the number of streams increases while their extent in fre-

quency space decreases. When the particles cross our location for the first time, they have not had enough time to become significantly spread in angle. We then observe only one big stream (left panel of Fig. 2). At some later time, particles with the highest frequencies begin to overtake the slowest ones and therefore we observe multiple streams (since the angles are periodic) each with its own characteristic frequency.

Since the orbital frequencies are constant (for a time independent gravitational potential) the location of a particle in frequency space remains unchanged. The changing pattern shown in Fig. 2 is simply a consequence of the fact that we restrict our analysis to particles at a given spatial location. The gaps thus correspond to particles which are located outside our window.

The network of patches is shaped by lines of constant frequency  $\Omega_i = cst$ . As a consequence, and because of the relation implied by Eq. (7), the distribution of particles in action space is also very regular. However, in general the relation between frequencies and actions will not be linear, and therefore the distribution of particles in action space is typically more complex (see e.g. Figure 6 below).

The number of clumps observed along each frequency direction at a given location can be estimated by considering the initial spread in the frequency. For example, at  $\Omega_2 = cst$ ,  $\Delta\Omega_1 = \Omega_1^{\max} - \Omega_1^{\min}$ . After some time  $t = t_3$ , the angle  $\theta_1$  between the particles with the largest and smallest  $\Omega_1$  has increased by an amount

$$\Delta\theta_1(t_3) = \Delta\Omega_1 t_3. \quad (8)$$

Since  $\theta_1$  is a  $2\pi$ -periodic variable the number of streams  $N_1$  at  $\Omega_2 = cst$  is

$$N_1 = \frac{\Delta\theta_1(t_3) + \Delta\theta_1(t_0)}{2\pi} \approx \frac{\Delta\theta_1(t_3)}{2\pi} \quad (9)$$

where the last approximation holds if  $t_3$  is long enough and hence  $\Delta\theta_1(t_3) \gg \Delta\theta_1(t_0)$ .

Another quantity of interest is the distance between two adjacent streams in frequency space,

$$\delta\Omega_i = \frac{\Delta\Omega_i}{N_i} = \frac{2\pi}{t}, \quad i = 1, 2. \quad (10)$$

The time  $t$  may be considered as the time of disruption of our system (i.e. its constituent stars have been tidally stripped, and move only under the influence of the host gravitational field). Eq. (10) states that this time can be directly estimated by measuring  $\delta\Omega_i$ . Moreover, systems will have different values of  $\delta\Omega_i$  depending on the time of disruption, which implies that this characteristic scale could be used to recognise the streams originating in objects accreted at different epochs.

### 3.2 Spherical potentials

We now turn our attention towards dynamical systems with an underlying spherical potential,  $\Phi(r)$ . Due to the conservation of angular momentum  $L$ , the motion of stars are constrained to remain in a plane, implying that there are only two independent frequencies of motion:  $\Omega_r$  associated to the radial oscillation and  $\Omega_\phi$  associated to the angular oscillation in this plane.

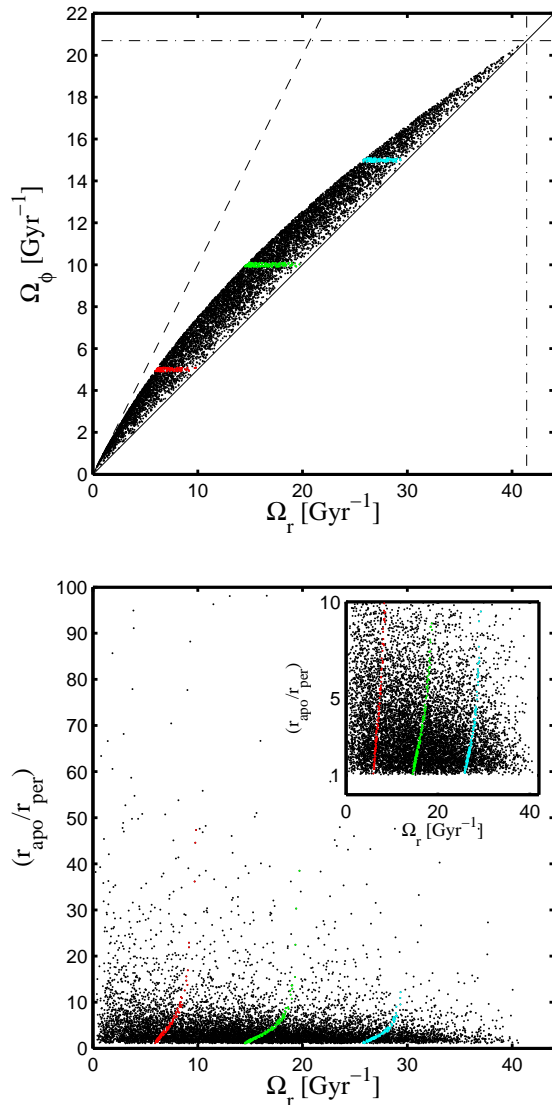


**Figure 3.** Top: Distribution of possible orbits in a Plummer sphere in frequency space. The solid line corresponds to  $\Omega_r = 2\Omega_\phi$ , as in the case of orbits in a homogeneous sphere. The dashed line shows  $\Omega_r = \Omega_\phi$ , as found for all orbits in a point mass distribution. The left wedge of the distribution corresponds to circular orbits. Bottom: Relation between the radial frequency  $\Omega_r$  and the orbital apocentre-to-pericentre ratio.

#### 3.2.1 Characterising frequency space

Our previous analysis has shown that the space of frequencies appears to be well suited to identify streams. Here we will characterise this space and how its properties depend on the form of the host gravitational potential.

The angular and radial periods of an orbit are related to the respective frequencies through

$$T_\phi = 2\pi/\Omega_\phi, \quad T_r = 2\pi/\Omega_r. \quad (11)$$

Once a radial oscillation is completed the azimuthal angle has increased by an amount  $\Delta\phi = \Omega_\phi T_r$  or, equivalently

$$\Delta\phi = 2\pi \frac{\Omega_\phi}{\Omega_r},$$

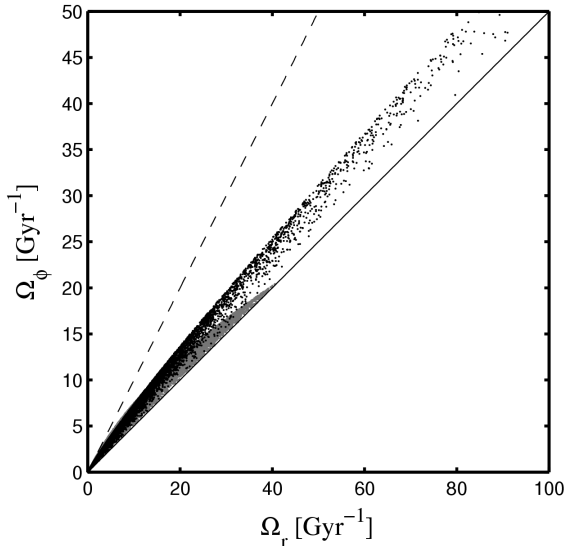


**Figure 4.** Distribution of possible orbits in a Hernquist profile (black dots) in frequency space. For comparison, the distribution for a Plummer sphere is shown in grey. Solid and dashed lines represent as before the natural limits of this space, i.e.  $\Omega_r = 2\Omega_\phi$  and  $\Omega_r = \Omega_\phi$  respectively. Note that because the Hernquist inner density profile is cusped orbits with high frequencies do not bend over to the boundary associated with the homogeneous sphere.

thus

$$\frac{\Omega_r}{\Omega_\phi} = \frac{T_\phi}{T_r} = \frac{2\pi}{\Delta\phi}. \quad (12)$$

In general  $2\pi/\Delta\phi$  will not be a rational number and therefore the orbit will not be closed. However there are two gravitational potentials in which all orbits are closed, those of an homogeneous sphere and of a point mass. Notice that any other spherical system may be considered to have a mass distribution between these limiting cases, i.e. its density gradient will be neither as shallow nor as steep as in these two cases. Orbits in a time-independent homogeneous mass distribution have  $\Delta\phi = \pi$ , whereas for the Kepler problem  $\Delta\phi = 2\pi$ . From Eq. (12) this implies that the frequencies of a bound orbit in any spherical mass distribution are constrained to lie inside the subspace defined by  $\Omega_r/2 \leq \Omega_\phi \leq \Omega_r$ . The extent to which this subspace is probed by orbits depends on the exact distribution of mass.

To examine this, let us consider the Plummer potential,  $\Phi$ , generated by a density  $\rho$ , where

$$\begin{aligned} \Phi(r) &= \frac{-GM}{\sqrt{r^2 + b^2}}, \\ \rho(r) &= \frac{3M}{4\pi b^3} \left(1 + \frac{r^2}{b^2}\right)^{-5/2} \end{aligned} \quad (13)$$

(Plummer 1911). We sample the frequency space in this potential by randomly drawing  $10^4$  orbits from the distribution function associated to the Plummer sphere with parameters  $M = 10^{12} M_\odot$  and  $b = 21.57$  kpc. The upper panel in Fig. 3 shows the distribution of these orbits in frequency space. The solid line and dashed lines correspond to  $\Omega_r = 2\Omega_\phi$  (homogeneous sphere) and  $\Omega_r = \Omega_\phi$  (point mass), respectively. Note that orbits with small frequencies cover the

whole region between these two lines. Instead, orbits with high frequencies tend to bend over towards the line given by the homogeneous sphere. This is because particles on orbits with low frequencies populate the outer regions of the system, and hence perceive a potential close to that of a point mass. On the other hand those on high frequency orbits are generally confined to the central regions of the system. Since the Plummer density profile has a core these particles will feel a potential resembling that of the homogeneous distribution. The sharp cut-off at a value of  $\Omega_r \approx 42 \text{ Gyr}^{-1}$  therefore corresponds to the characteristic frequency associated to the homogeneous mass distribution, i.e. for  $r \ll b$ , a particle in the Plummer model should have a period of  $T_r \sim \sqrt{\frac{\pi^2 b^3}{GM}}$  which in our case corresponds to 0.15 Gyr, or  $\Omega_r = 42 \text{ Gyr}^{-1}$ .

For a given  $\Omega_\phi$ , (nearly) circular orbits will be those with the largest radial period, i.e. the smallest  $\Omega_r$  frequency. Thus such orbits are located on the wedge seen in the top panel of Fig. 3. This is also illustrated in the bottom panel of the same figure, where we have plotted the ratio of apocentre to pericentre distances of orbits as a function of  $\Omega_r$ . As we can see, orbits with the lowest  $\Omega_r$  for a given  $\Omega_\phi = cst$  have  $r_{\text{apo}}/r_{\text{per}} = 1$ .

We now consider a system with a cuspy density distribution, namely the Hernquist profile whose potential,  $\Phi$ , and density  $\rho$ , are given by

$$\begin{aligned} \Phi(r) &= \frac{-GM}{r+b}, \\ \rho(r) &= \frac{bM}{2\pi r} \frac{1}{(r+b)^3} \end{aligned} \quad (14)$$

(Hernquist 1990). We set  $M = 10^{12} M_\odot$  and  $b = 21.57$  kpc. As before, we sample the available phase-space with  $10^4$  orbits. The black points in Fig. 4 show the resulting distribution of orbits in frequency space. For comparison, we overplotted the frequencies for the Plummer profile (in grey). At the low frequencies end both distributions overlap as expected (point mass regime). However there is a significant difference in the region populated by orbits with high frequencies. Due to the lack of a core in the Hernquist density distribution, the bend over towards  $\Omega_r = 2\Omega_\phi$ , i.e. the regime of the homogeneous mass distribution, has disappeared, and there is no upper limit to the radial or angular frequency of motion.

### 3.2.2 Comparing different projections of phase-space

Various spaces have been proposed to identify debris from disrupted satellites. For example, Helmi & de Zeeuw (2000) introduced the space of energy, total angular momentum and its  $z$ -component ( $E, L, L_z$ ). Later on, Helmi et al. (2006) show that substructure can be identified by looking at the apocentre, pericentre and  $L_z$  space. In this space, streams are represented by extended structures, roughly along a line of constant eccentricity. In this section we will compare the distribution of debris in these and other previously used spaces to that in the frequency space. To this end we consider the accretion of a satellite galaxy onto a spherical host.

We represent the host with the Plummer profile discussed in the previous section. The satellite is assumed to be spherical and to have an isotropic velocity ellipsoid, and

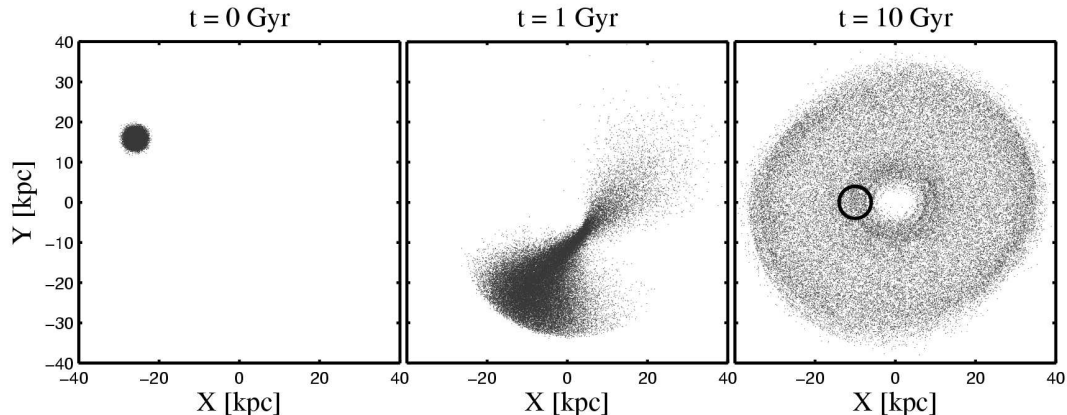


**Figure 5.** X-Y distribution of particles from an accreted satellite at three different times, as indicated on each panel. The black circle shows the location of a “Solar neighbourhood” sphere.

is modelled with a multivariate Gaussian in 6D with a dispersion of  $\sigma_x = 1.1$  kpc and  $\sigma_v = 22$  km/sec. We set the central particle of the satellite on an orbit with apocentre  $r_{\text{apo}} = 35.4$  kpc and pericentre  $r_{\text{per}} = 7.76$  kpc. We follow then the evolution of the satellite for approximately 10 Gyr. For simplicity, in this experiment the self-gravity of the satellite is not considered. As a consequence, we expect to find a larger number of streams at any given epoch, with a larger spread in orbital parameters, in comparison to the self-gravitating case. This is because particles can drift apart right from the start, whereas when their self-gravity is considered, this will only happen during successive pericentric passages where they are (typically) stripped from the parent satellite.

In Fig. 5 we show the spatial distribution of satellite particles at three different times. To study the distribution of particles in various projections of phase-space we focus on those inside a sphere of radius 4 kpc centred at  $r = 10.5$  kpc at the final time, as shown in the rightmost panel of this Figure.

The results are shown in Fig. 6 for six different spaces. Grey points represent all the particles of the satellite whereas black points only those inside the sphere of interest. In the top left corner (panel a) we show their projection in frequency space. As in the toy model discussed in Section 3.1, for a given  $\Omega_\phi = cst$  we find multiple streams in  $\Omega_r$ . Note that there are typically more streams at constant  $\Omega_\phi$  than at constant  $\Omega_r$ . This is because  $T_r \leq T_\phi \leq 2T_r$ , and hence mixing occurs faster in the  $r$ -direction.

Notice that some of the groups of particles found at given  $\Omega_r$  and  $\Omega_\phi \approx cst$  may be decomposed into smaller structures. This can be understood from the radial velocity vs. radial distance plot shown in the bottom right panel of Fig. 6. Streams with pericentres inside the sphere under consideration, appear in frequency space as a single compact structure. For the rest we observe two separate structures, each of these associated to particles located just before or after their corresponding pericentre.

The top right panel of Fig. 6 shows the distribution of particles in a projection of velocity space. Although several features are visible, the individual streams are clearly less

well separated than in panel a). This is also the case for the radial velocity vs. radial distance plot (panel f).

The two middle panels of Fig. 6 show the distribution of particles in the  $E - L_z$  (left) and apocentre vs. pericentre (right) spaces. The number of structures in the  $E - L_z$  space is smaller and slightly less sharp than in frequency space. On the other hand, streams are well detached from each other in the apocentre vs. pericentre space. Finally, in the bottom left panel we show the distribution of particles in the space of actions,  $J_r$  vs.  $J_\phi$ . As in the  $E - L_z$  space, distinction of the various streams is less clear in this space, and hence it appears to be less suitable for finding individual debris streams.

This analysis shows that frequency space is probably the best space to identify streams associated to accretion events.

### 3.2.3 Estimating the time of accretion

As discussed before the separation between adjacent streams along each direction of the space of orbital frequencies yields a direct estimate of the time of infall, e.g. a satellite accreted 10 Gyr ago should give rise to streams separated by a scale  $\delta\Omega_r = \delta\Omega_\phi = 2\pi/10 \text{ Gyr}^{-1}$ .

In this section we develop a method to measure this separation. As an example we focus on the streams shown in panel a) of Fig. 6. Because there is a unique scale (all streams are separated by the same amount) a straightforward way to compute this separation is to use Fourier analysis techniques. We proceed by first creating an image from the scatter plot in frequency space, to which we then apply a Fourier transform. In the final step we compute the power spectrum. To obtain an image from our data we grid the frequency space with a regular  $N \times N$  mesh of bin size  $\Delta$  in both  $\Omega_r$  and  $\Omega_\phi$  directions. In this way, the number of particles in the  $(n_r, n_\phi)$  bin of the grid is  $h(n_r, n_\phi)$ . We apply a two dimensional discrete Fourier transform to this image:

$$H(k_r, k_\phi) = \sum_{n_r=0}^{N-1} \sum_{n_\phi=0}^{N-1} \exp(2\pi i k_r n_r / N) \exp(2\pi i k_\phi n_\phi / N) h(n_r, n_\phi), \quad (15)$$

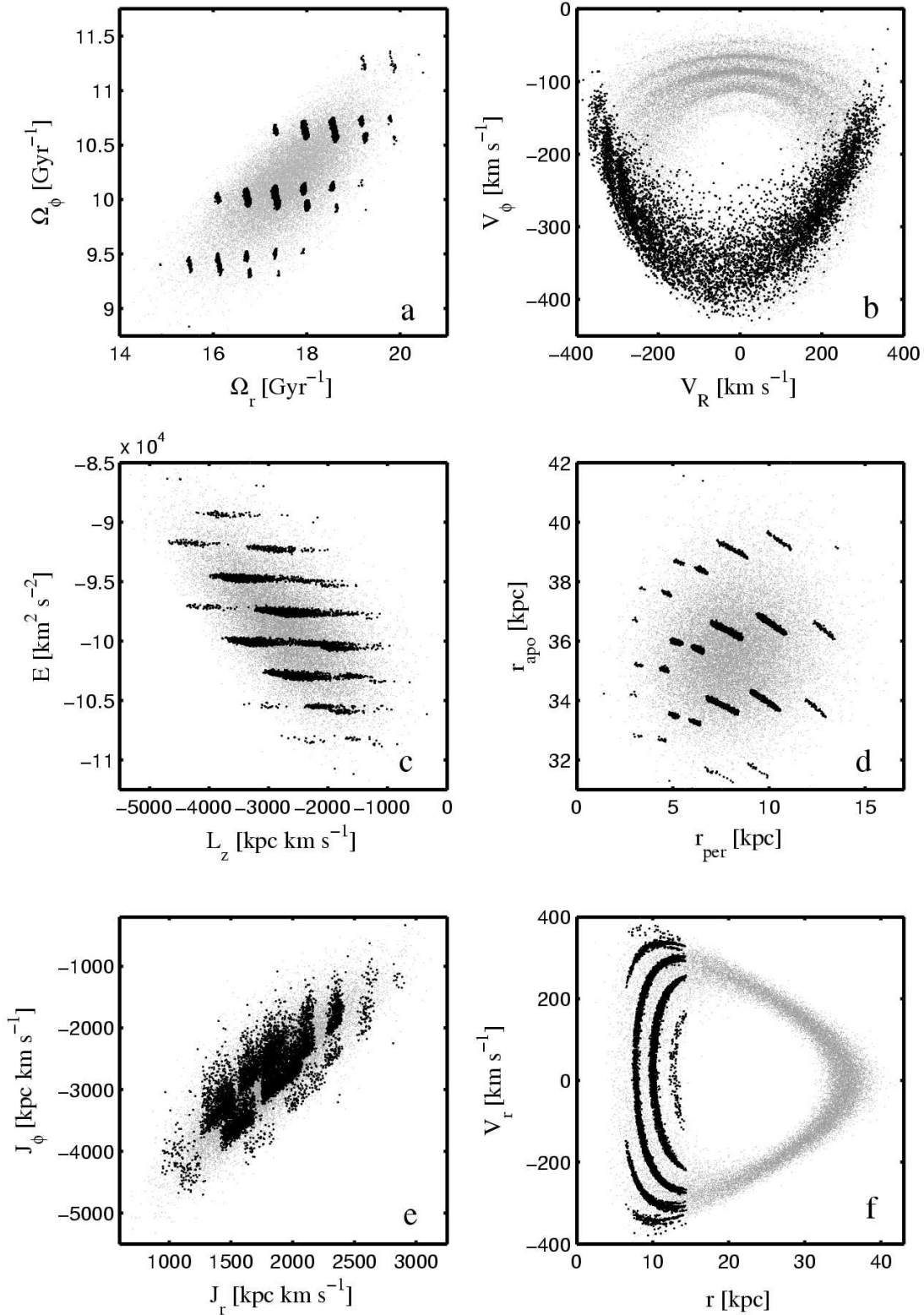


**Figure 6.** Comparison of the various spaces commonly used to identify merger debris. Grey dots show the distribution of all satellite particles whereas the black dots represent the particles inside the sphere shown in Fig. 5. As in the toy model example discussed in Section 3.1, streams in frequency space (top left panel) are distributed in a regular pattern. Notice that the distribution of particles in the frequency space is much better defined than in any other of the spaces considered.

with  $k_r, k_\phi = -\frac{N}{2}, \dots, \frac{N}{2} - 1$ .

In the top panel of Fig. 7 we show the image of the panel a) of Figure 6 in Fourier space. This has been computed on a grid of 200 by 200 elements. The axes represent the wavenumbers in each direction ( $k_r, k_\phi$ ) while the colour coding show the square value of each of the Fourier components  $|H(k_r, k_\phi)|^2$ . As we can see from this image, and as expected from our previous discussion, a regular pattern is present. To measure the characteristic scale we consider two different “slits” (of width  $\Delta = 4$  bins) of the Fourier image around  $k_r = 0$  and  $k_\phi = 0$ . These regions are delimited by the black lines in the top panel of Fig. 7. We can now compute the one-dimensional power spectrum of the image along each direction as

$$\begin{aligned} P(0) &= \frac{1}{N^2} |H(0,0)|^2, \\ P(k_r) &= \frac{1}{N^2} [|H(k_r,0)|^2 + |H(-k_r,0)|^2] \\ &\text{for } k_r = 1, \dots, \left(\frac{N}{2} - 1\right), \end{aligned} \quad (16)$$

$$P(N/2) = \frac{1}{N^2} |H(-N/2,0)|^2$$

and analogously for  $P(k_\phi)$ . Recall that the one-dimensional power spectrum we compute is, in practise, an average over the slits considered along the  $k_r$  and  $k_\phi$  directions.

The results are shown in the middle and the bottom panels of Figure 7, for  $P(k_r)$  and  $P(k_\phi)$ , respectively. The scales present in the power spectrum  $P(k_r)$  are associated to separations in the  $\Omega_r$  direction (since they correspond to  $k_\phi = 0$ ). The large power for frequencies close to zero, i.e.  $P(0)$  represents the average power over the whole image. All other peaks in the spectrum are related to waves resonating with our image. In particular the first peak, with the highest power, is associated to a frequency of  $f_0 = 1.59$  Gyr, and is denoted by the vertical black line in the spectrum. The corresponding wavelength of this peak is  $0.62 \text{ Gyr}^{-1} \approx 2\pi/10 \text{ Gyr}^{-1}$ . This is in fact the separation we would have estimated using Eq. (10). The rest of the peaks in the spectrum are associated to the harmonics of this frequency, i.e.,  $2f_0, 3f_0$ , etc.

The situation is similar when we consider a cut around  $k_r = 0$ . In this case the scales present in the power spectrum are associated to separations in the  $\Omega_\phi$  direction. We find the peak with the highest amplitude to be at the same frequency  $f_0$  and it is possible to distinguish some of its harmonics. However, due to the smaller number of streams we have in the  $\Omega_\phi$  direction, the peaks are less clearly defined than for  $P(k_r)$ .

#### 4 FREQUENCY SPACE FOR TIME DEPENDENT POTENTIALS

In a hierarchical universe, the gravitational potentials associated to galaxies are expected to have changed in time. Under these circumstances, quantities such as the energy, apocentre and pericentre and also the frequencies of individual orbits will no longer be conserved. It is therefore of special interest to study how a time dependent potential affects the structure of debris in frequency space.

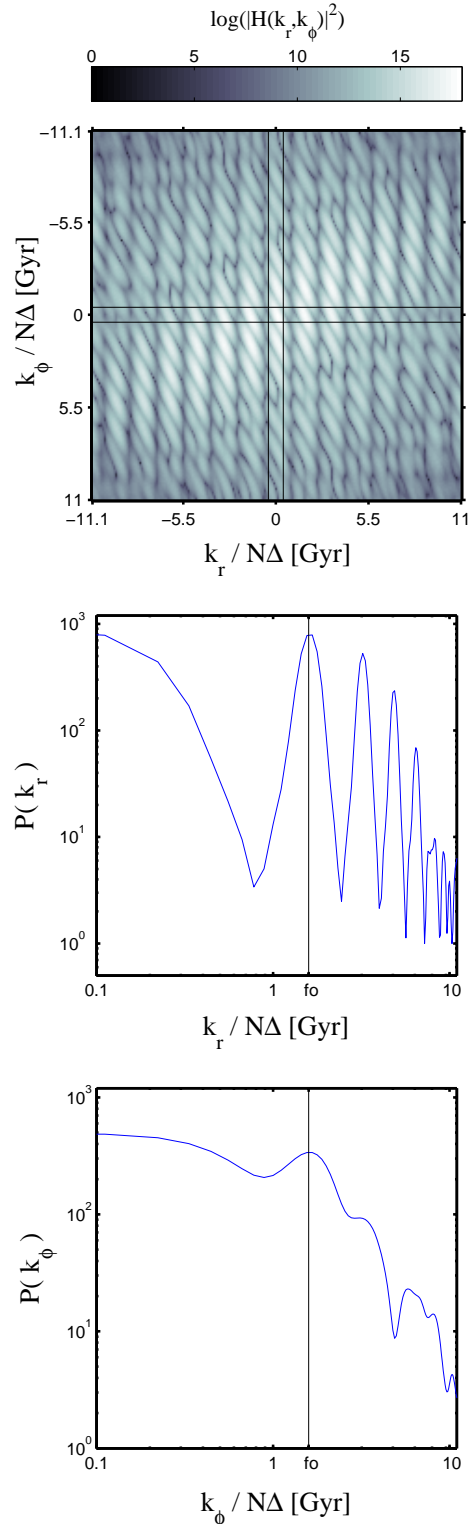


**Figure 7.** Top panel: Fourier transform of the distribution of streams shown in the top left panel of Fig. 6. The black lines denote the regions selected in the Fourier image to compute the 1-d power spectra, i.e. around  $k_\phi = 0$  (middle panel) and  $k_r = 0$  (lower panel). The black vertical lines in these panels show the location of the peak with the highest power in the spectrum.



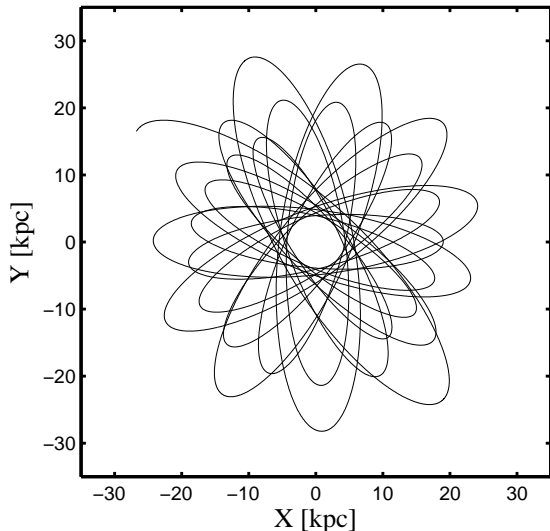


**Figure 8.** Evolution of an orbit in a time dependent Plummer potential whose mass varies as  $M = M_0 e^{t/t_{\text{scale}}}$ .

To this end, we consider a simple model of a satellite accreted onto a Plummer sphere whose mass varies according to

$$M(t) = M_0 \exp(t/t_{\text{scale}}) \quad (17)$$

where we explore several values for the time scale,  $t_{\text{scale}}$ . An example of an orbit in this potential is shown in Fig. 8. In this case,  $t_{\text{scale}} = 3.3$  Gyr,  $M_0 = 10^{12} M_{\odot}$  and  $b = 21.57$  kpc. From this Figure we see that as the mass of the system increases, the orbit shrinks in extent, and consequently has a shorter period.

#### 4.1 Time evolution of the frequencies and the rate of change of the potential

To derive the evolution of the frequencies of motion for an orbit such as that shown in Fig. 8, we proceed as follows. At each step of this orbit’s time-integration, we take the instantaneous position and velocity as initial conditions to compute an orbit in the instantaneous (frozen) potential. Then, for this orbit we derive an instantaneous set of frequencies.

We will consider the evolution of two different orbits: an initially outer orbit with an apocentre of  $r_{\text{apo}} = 64$  kpc and pericentre of  $r_{\text{per}} = 19$  kpc, and a second inner orbit with  $r_{\text{apo}} = 24.6$  kpc and  $r_{\text{per}} = 4.7$  kpc. The initial values of the frequencies of the outer orbit are  $\Omega_r = 8.1 \text{ Gyr}^{-1}$  and  $\Omega_{\phi} = 5.77 \text{ Gyr}^{-1}$ , whereas for the inner one they are  $\Omega_r = 24.7 \text{ Gyr}^{-1}$  and  $\Omega_{\phi} = 13.28 \text{ Gyr}^{-1}$ .

Let us first consider a slowly varying potential, where  $t_{\text{scale}} = 30$  Gyr. We follow the evolution of the orbit during 14 Gyr. The top panel in Fig. 9 shows the time evolution of the radial action  $J_r$  for this case, where black and light-grey lines in this figure correspond to the outer and the inner orbit respectively. This Figure shows that the instantaneous

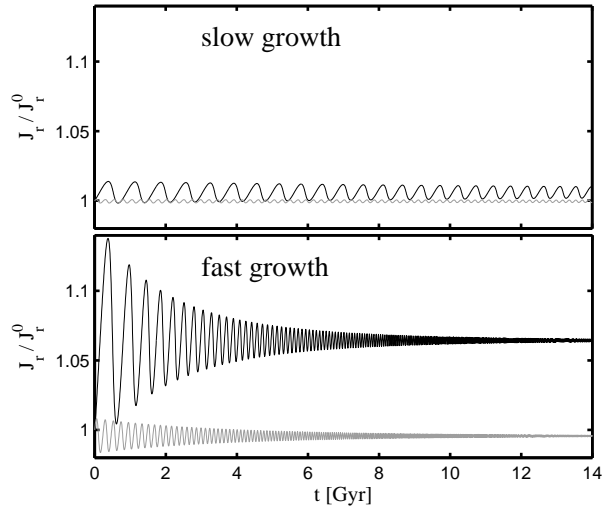


**Figure 9.** Time evolution of the radial action of two different orbits in a very slow (top panel) and a very fast (bottom panel) time varying Plummer potentials. The black and light-grey curves correspond to an outer and an inner orbit respectively. The observed oscillatory behaviour is related to the orbital motion.

action  $J_r$  displays an oscillatory behaviour<sup>1</sup>, with a period that corresponds to the period of the orbit.

This is not surprising since under adiabatic variations of the potential it is the time average of the actions that remains constant (see Goldstein, Poole & Safko 2001; Wells & Siklos 2006). In general, for a given orbit the amplitude of the oscillation depends on the time scale on which the potential grows. By increasing  $t_{\text{scale}}$  the evolution is more adiabatic and the amplitude of the oscillation is decreased.

In order for an orbit to be in a condition of adiabatic invariance it is necessary that  $t_{\text{orb}} \ll t_{\text{scale}}$ , where  $t_{\text{orb}}$  is the orbital period. Since inner orbits have shorter orbital periods, we expect those to behave “more adiabatically” compared to outer orbits. This is demonstrated in the top panel in Fig. 9, where the amplitude of the oscillation of  $J_r$  is smaller for the inner orbit. In addition, in this case, the final average value of  $J_r$  is more similar to the initial value.

Let us now consider  $t_{\text{scale}} = 3$  Gyr, i.e. a rapidly growing potential. The evolution of  $J_r$  for the same initially outer and inner orbits is shown in the bottom panel of Fig. 9. Clearly the final values of the radial action  $J_r$  are now very different from the initial ones, especially in the case of the outer orbit. This is because this orbit is not in an adiabatic regime (the initial radial period is  $T_r = 0.78$  Gyr which is comparable to  $t_{\text{scale}}$ ). A second feature that is clearly present is the damping in the amplitude of the oscillation. Since the mass of the system grows in time, orbits are continuously driven towards deeper regions of the potential well, implying that the corresponding orbital periods decrease with time. Therefore what we observe is a transition from a non-adiabatic towards an adiabatic regime.

In Figure 10 we focus on the evolution of the radial fre-

<sup>1</sup> Note that due to the spherical nature of the potential the other two actions, associated with the angular momentum, remain constant in time.

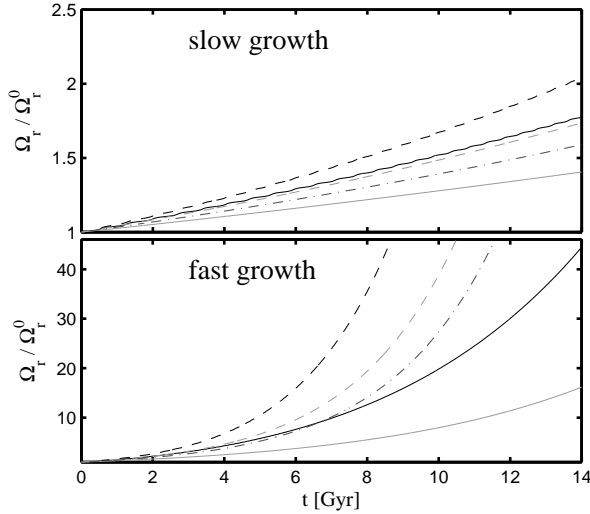


**Figure 10.** Time evolution of the radial frequency for two different orbits in a very slow (top panel) and a very fast (bottom panel) time varying Plummer potentials. The black and light-grey curves correspond to an outer and an inner orbit respectively. The dashed lines represent the time evolution of the normalised energies of each orbit  $E/E_0$ , while the dotted-dashed line shows the time evolution of the mass of the host  $M/M_0$ .

quency  $\Omega_r$  (the angular frequency  $\Omega_\phi$  depicts a qualitatively similar behaviour). The top and bottom panels of this Figure correspond, respectively, to the slowly and to the rapidly varying potentials. Note that in contrast to the actions, the frequencies do change with time, and that their evolution appears to follow closely that of the potential. For comparison, we plot in Fig. 10 the time evolution of the normalised energy of each orbit  $E/E_0$  (dashed lines), and of the mass of the system  $M/M_0$  (dotted-dashed line).

The exact relation between the evolution of the frequencies and that of the potential can not be derived analytically in the general case. However, some insights may be obtained from two simple cases: the homogeneous sphere and the Kepler potentials.

For the homogeneous sphere the radial period  $T_r \propto \rho^{-\frac{1}{2}}$  or  $T_r \propto M^{-\frac{1}{2}}$  (Binney & Tremaine 2008), therefore  $\Omega_r \propto M^{\frac{1}{2}}$ . Hence, for  $M(t) \propto \exp(t/t_{\text{scale}})$  we obtain

$$\Omega_r(t) \propto \exp(t/2t_{\text{scale}}). \quad (18)$$

Therefore, the frequencies evolve in time with the same functional form as the potential, but on a time scale that is twice as long. Consequently, their evolution is slower.

In a Kepler potential the radial orbital frequency of a particle is

$$\Omega_r = \sqrt{\frac{GM}{a^3}} \quad (19)$$

where  $a = L^2 / [GM(1 - e^2)]$  is the semi-major axis of the orbit and  $e = CL^2/GM$  its eccentricity. Here  $C$  is an arbitrary constant.

Differentiating Eq. (19) with respect to time and replacing  $\dot{a} = -aM(1 + e^2)/M(1 - e^2)$  we have

$$\dot{\Omega}_r = \frac{1}{2}\Omega_r \left( \frac{\dot{M}}{M} + 3\frac{\dot{M}}{M} \frac{1 + e^2}{1 - e^2} \right). \quad (20)$$

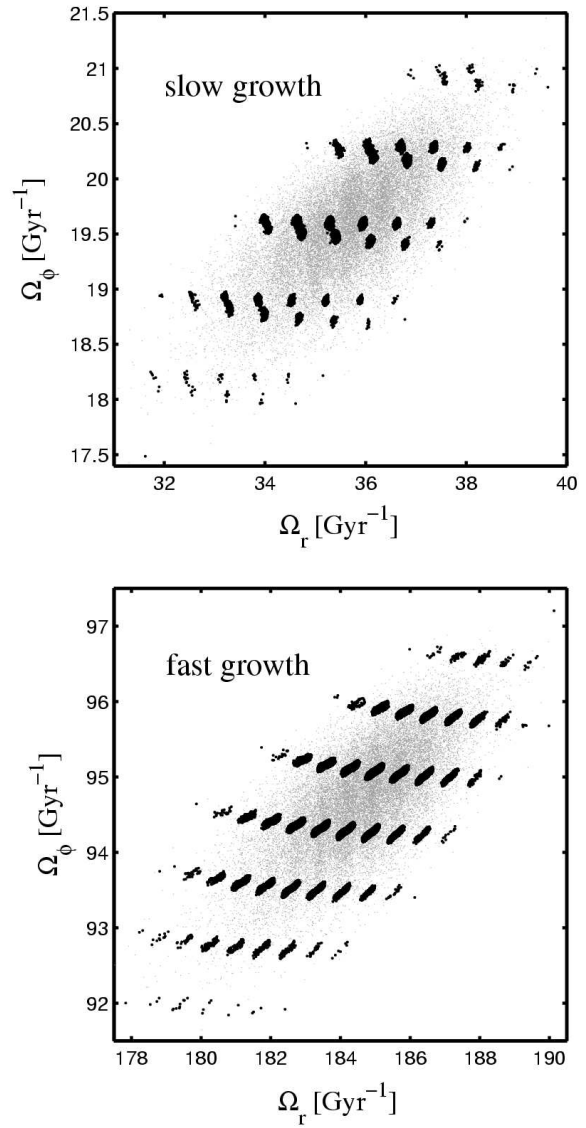


**Figure 11.** Distribution of particles in frequency space located inside a sphere of 4 kpc radius at 10.5 kpc from the centre of the time-dependent Plummer sphere after 10 Gyr of evolution. The timescales for the mass growth of the Plummer sphere are  $t_{\text{scale}} = 12$  Gyr (top panel) and  $t_{\text{scale}} = 3$  Gyr (bottom panel). Note that structure in frequency space is not destroyed by the time varying nature of the potential.

Since we may express the eccentricity as  $e = e_0 M_0/M$ , we can solve Eq. (20) to obtain

$$\Omega_r(t) = \frac{\Omega_{r,0} \exp(2t/t_{\text{scale}}) - e_0^2}{1 - e_0^2 \exp(t/t_{\text{scale}})}. \quad (21)$$

Again, in this example we find that frequencies are evolving in a similar fashion as the potential. Therefore a very external orbit in the Plummer sphere should initially evolve at a rate similar to that given by Eq. (21) (as for the Kepler potential). On the other hand, inner orbits should evolve at a rate similar to that of the homogeneous sphere. Thus, we can already see that orbits in a given potential will evolve at

different rates, depending on their initial location in phase-space.

## 4.2 Structure in frequency space

In this section we address how the debris of a satellite is distributed in frequency space in the time-dependent Plummer potential discussed above.

We ran simulations with the same satellite and orbital initial conditions as described in Section 3.2.2. We followed its evolution in the Plummer potential with two different timescales, namely  $t_{\text{scale}} = 3$  Gyr and 12 Gyr. As before, we do not include the self-gravity of the satellite.

Fig. 11 shows the distribution of particles inside a sphere of 4 kpc radius located at 10.5 kpc from the centre of the system after 10 Gyr of evolution. The top panel presents the results for  $t_{\text{scale}} = 12$  Gyr while the bottom panel corresponds to  $t_{\text{scale}} = 3$  Gyr. As we can see from this Figure, even in a time dependent system, satellite debris at a given spatial location is distributed in a regular pattern of patches in the space of orbital frequencies.

In the simulation where the time evolution is slow (i.e.,  $t_{\text{scale}} = 12$  Gyr) some of the structures may be decomposed into two clumps. As we explained in Section 3.2.2, such structures appear when neither the apocentre nor the pericentre of the orbits fall inside the sphere under consideration. In contrast, when the potential evolves quickly the particles in each stream are all distributed in compact single structures. This is because in this case the orbits have shrunk so much after 10 Gyr that all streams present in this volume have their apocentres inside the chosen sphere.

Comparison to the case in which the potential is fixed (Fig. 6) shows that streams in the  $\Omega_r$  direction are not exactly distributed along a line of  $\Omega_\phi = cst$  but rather on a line with a given curvature. This is due to the fact that orbits with different initial frequencies evolve at different rates (as discussed in the previous section).

Furthermore, the extent of the distribution of particles in frequency space has also changed depending on the timescale of variation of the potential. For example, for the case in which the potential is growing on a timescale of 12 Gyr we find that the total extent of the system in the  $\Omega_r$  direction (considering all  $\Omega_\phi$ ),  $\Delta\Omega_r = \max(\Omega_r) - \min(\Omega_r) = 8.7 \text{ Gyr}^{-1}$  whereas for the case in which  $t_{\text{scale}} = 3$  Gyr  $\Delta\Omega_r = 12.8 \text{ Gyr}^{-1}$ .

We may conclude from these experiments that the time evolution modelled here for the host potential does not destroy the coherence of satellite debris in frequency space. Furthermore, since the frequencies evolve at different rates even for particles with same origin, it may be possible to recover the evolution of the host potential, for example, by measuring the curvature of the lines over which the streams are distributed in frequency space. Note that this implies that the host's evolution has left its imprints in the present day orbits of accreted stars. This is in contrast to the results by Peñarrubia et al. (2006) (see also Warnick et al. 2008), who find that present-day observables only constrain the present day mass distribution of the host, independently of its past evolution.

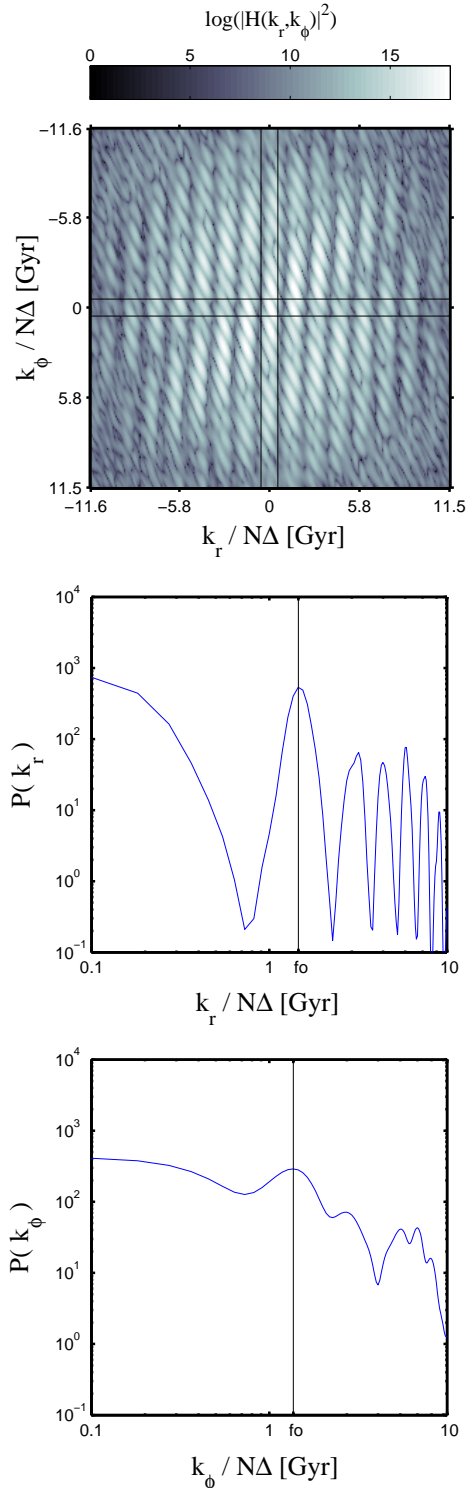


**Figure 12.** Top panel: Fourier transform of the distribution of streams shown in the top panel of Fig. 11. As in Fig. 7 the middle and central panels depict the 1-d power spectra along the  $k_r$  and  $k_\phi$  directions, respectively. The location of the first peak (denoted by the vertical lines in these panels) can be used to estimate the accretion time of the satellite.

### 4.3 Estimating the time of accretion

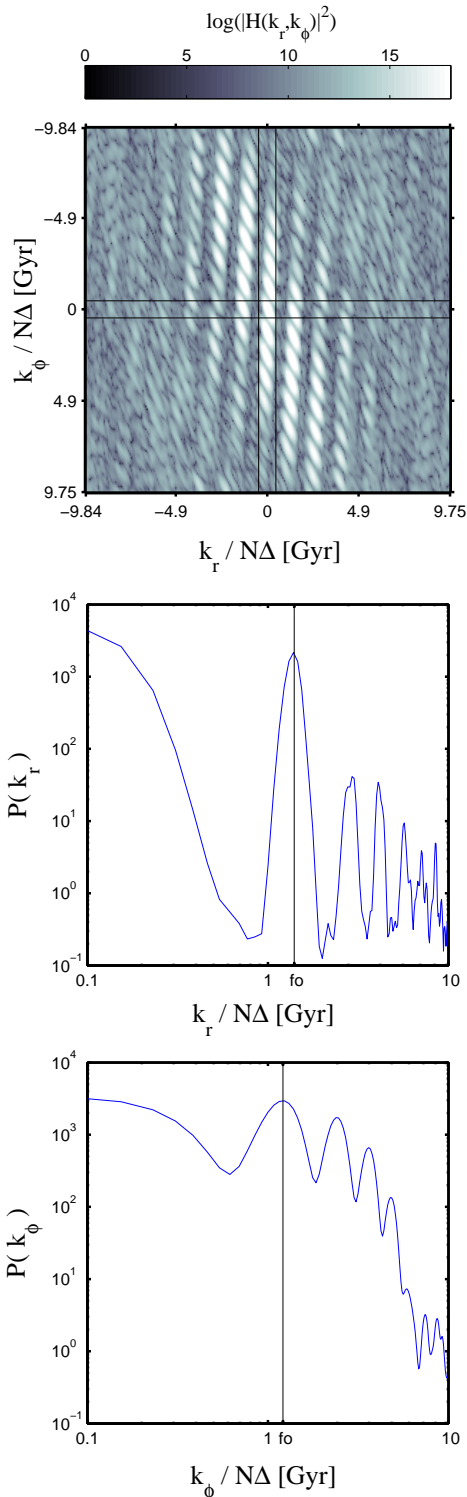
The top panel in Fig. 12 shows the results of applying a two dimensional Fourier transform to an image created from distribution of streams shown in the top panel of Fig. 11. This corresponds to the satellite accreted 10 Gyr ago onto a host whose mass increases on  $t_{\text{scale}} = 12$  Gyr. As before we compute the power spectrum along the  $k_\phi$  and  $k_r$  directions. The middle panel shows  $P(k_r)$ , and the black line here denotes the location of the peak with the highest amplitude, having a wavenumber of  $f_0 = 1.46$  Gyr. From this spectrum we would estimate the satellite was accreted 9.2 Gyr ago. When  $P(k_\phi)$  is considered, the highest amplitude peak is located at a wavenumber  $f_0 = 1.36$  Gyr, corresponding to an estimated time of accretion of 8.6 Gyr. Therefore, in this example the analysis of the power spectrum suggests different times of accretion depending on whether  $\Omega_r$  or  $\Omega_\phi$  are considered. Both values are reasonably close to the actual accretion time (10 Gyr ago), but the direction associated to  $\Omega_r$  appears to provide a better estimate.

Fig. 13 shows the same result but now for the satellite accreted onto a host potential that evolves on  $t_{\text{scale}} = 3$  Gyr.  $P(k_r)$  peaks at a frequency  $f_0 = 1.4$  Gyr, as shown by the black line in the middle panel of this Figure while  $P(k_\phi)$  peaks at a frequency  $f_0 = 1.21$  Gyr. The corresponding estimated times of accretion are 8.8 and 7.6 Gyr, respectively. Note that even though the potential evolves on a very short timescale, the estimated accretion times only differ by  $\sim 15 - 25\%$  from the true value.

The timescales derived in this way will always provide lower limits to the actual time of accretion. This is because if  $N_r$  streams are observed at time  $t_f$  in frequency space (at a constant  $\Omega_\phi$ ), then  $t_{\text{acc}}/2\pi = 1/\delta\Omega_r(t_f) = N_r/\Delta\Omega_r(t_f) < N_r/\Delta\Omega_r(0)$ .

## 5 FULL N-BODY CASE

The previous analysis has shown that frequency space is particularly well suited for identifying streams from mergers, at least for the idealised potentials considered thus far. We now explore a more realistic case, namely that of a minor merger with a live host. We use one of the simulations of Villalobos & Helmi (2008) (hereafter VH08), that model the formation of a thick disk via the merger of a relatively massive satellite onto a pre-existing thin disk. Two important physical processes take place during the merger which may affect the structure of the debris in frequency space. First, the satellite suffers significant dynamical friction. Secondly, the host system responds strongly to the perturber, resulting in a disk that has been significantly tilted and heated. This implies that, even though the total mass of the system is conserved, its distribution evolves in time. The VH08 simulation that we consider here corresponds to a two component satellite (stars + dark matter) launched on a  $30^\circ$  inclination orbit with respect to the disk from a distance of approximately 84 kpc ( $\sim 50$  disk scale lengths). The host consists of a (live) dark halo and a (live) thin disk. The total (and the stellar) mass ratio between the satellite and the host is 20%. After 4.5 Gyr of evolution, the satellite is fully disrupted and has deposited debris in the disk of the host. The host disk is significantly thickened by this process and shows characteristics typical of thick disks.



**Figure 13.** Top panel: Fourier transform of the distribution of streams shown in the bottom panel of Fig. 11. As in Fig. 7 the middle and central panels depict the 1-d power spectra along the  $k_r$  and  $k_\phi$  directions, respectively, and the location of the first peak can be used to estimate the accretion time of the satellite.

### 5.1 Computing the frequencies

The remnant system modelled by VH08 does not have a separable gravitational potential which prevent us from deriving explicitly the action-angles variables using Eq. (2)-(3). Nevertheless several methods have been developed to obtain the frequencies of orbits in general potentials. Here we focus on the spectral analysis approach, introduced by Binney & Spergel (1984), which relies on the numerical integration of the equations of motion in a given potential. The basic idea is to perform a Fourier transform of the time series  $\mathbf{x}(t)$  (i.e., the orbit), and then to derive the frequencies of motion.

To obtain a reliable Fourier spectrum the orbits must be integrated for a very large number of periods. However, in the problem under consideration the orbits are not stationary, i.e. the frequencies are time dependent and so this approach cannot be applied directly using the orbits from the N-body simulation. This is why we have used the final output of the simulation to define a set of initial conditions which we integrate in a fixed (static) potential. This potential is an approximation of the final gravitational potential in our simulation. For simplicity we have taken a two component model, consisting in a Miyamoto-Nagai disk (Miyamoto & Nagai 1975)

$$\Phi_{\text{disk}} = -\frac{GM_{\text{disk}}}{\sqrt{R^2 + (a + \sqrt{z^2 + b^2})^2}}, \quad (22)$$

and NFW dark matter halo (Navarro, Frenk & White 1996)

$$\Phi_{\text{halo}} = -\Phi_0 \frac{r_s}{r} \log\left(1 + \frac{r}{r_s}\right). \quad (23)$$

We have set the parameters of the model to  $M_{\text{disk}} = 2.5 \times 10^{10} M_{\odot}$ ,  $a = 1.8$  kpc and  $b = 0.6$  kpc;  $\Phi_0 = 1.05 \times 10^5 \text{ km}^2 \text{ s}^{-2}$  and  $r_s = 14.1$  kpc. These choices lead to a density distribution that follows that of our simulation up to a radius of 50 kpc, which is large enough to enclose the apocentres of most particles presently found in a volume resembling the Solar neighbourhood. We thus integrate the orbits of the stellar particles located in such a volume for approximately 100 orbital periods and compute their frequencies using the code developed by Carpintero & Aguilar (1998). Although we have taken some care to find an approximation to the final potential that closely resembles that of the simulation, we do not expect significant changes in the substructure present in frequency space for other reasonable choices of the gravitational field. This is because we always focus on small volumes in space and hence small changes in the potential essentially act as a zero point offset and affect all particles present in this volume in the same way.

### 5.2 Results

In Fig. 14 we present the distribution of stellar particles inside a sphere of 2 kpc radius located at 8 kpc from the centre of the remnant galaxy in some commonly used spaces to identify substructure. Here the grey particles represent those originally present in the disk, while those from the satellite are colour-coded in black. The total number of stellar parti-

cles inside this sphere is approximately 27000, out of which 23000 belong to the satellite and 4000 to the host<sup>2</sup>.

The top panel of Fig. 14 shows the distribution of particles in the  $\Omega_{\phi}$  vs.  $\Omega_r$  space. Note the large amount of substructure present. As expected, satellite particles are distributed in multiple lumps associated with the different streams crossing this volume. These lumps are better defined in the region of orbits with low frequencies. This is because such orbits are more external and hence have longer mixing timescales.

The upper envelope defined by the smallest  $\Omega_r$  at a given  $\Omega_{\phi}$  corresponds to particles with low eccentricity (i.e. on more circular orbits) as discussed in Section 3.2.1. In our simulation this region is preferentially populated by disk particles.

In general, orbits in axisymmetric potentials have three independent frequencies: the previously discussed  $\Omega_r$  and  $\Omega_{\phi}$  and a third frequency associated with the vertical motion,  $\Omega_z$ . However, particles in the thick disk typically have very short periods in the vertical direction. Hence, the amount of streams expected in the  $\Omega_z$  direction is very large and therefore it is hard to resolve in our simulation, and not discussed further here.

In the bottom left panel of Fig. 14 we can observe the distribution of particles in the space defined by orbital apocentre and pericentre. The stripy features along lines of different eccentricities are the counterparts of the lumps located on diagonal lines in frequency space. The middle panel shows the  $E - L_z$  space, where extended structures with slightly different orientations may be seen. The panel on the right shows a projection of velocity space, which clearly exhibits less well-defined structures in comparison to the other spaces discussed. In general, we may conclude from this Figure that streams are much better defined and easier to interpret in frequency space than in any of the other projections considered.

### 5.3 Estimating the time of accretion

In comparison with the idealised cases discussed in Section 3.2.2 and 4.2 the distribution of particles in frequency space for the VH08 simulation is less regular. Nevertheless, we would like to explore if it is still possible to obtain a good estimation of the time of accretion of the satellite, using the Fourier analysis described in previous sections.

The top panel of Fig. 15 plots the image in Fourier space of the frequency plane  $\Omega_{\phi}$  vs.  $\Omega_r$  discussed above. This image was obtained by making a grid in frequency space and counting the number of particles in each grid element. As before the black lines in the top panel of Fig. 15 denote the cuts around  $k_r = 0$  and  $k_{\phi} = 0$  made to compute the 1-dimensional power spectra.

To estimate the uncertainties in the power spectrum, we create a second image obtained by assuming that the particles are spread throughout the permitted regions of frequency space according to a Poisson distribution. That

<sup>2</sup> This is due to higher number of particles used to simulate the satellite to properly resolve its structure in phase-space. Therefore, in practise only 1 in 50 satellite particles should be considered.

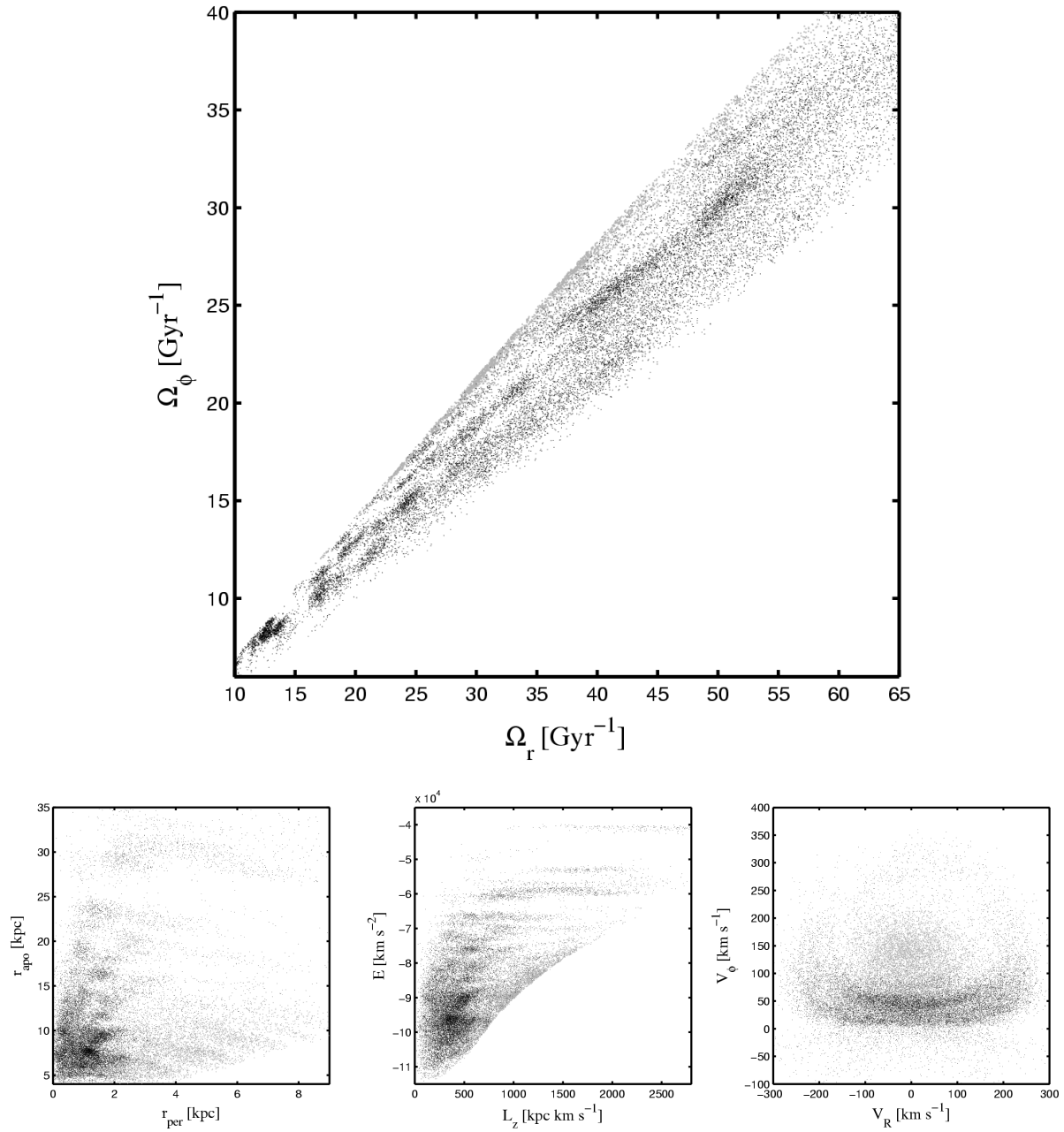


**Figure 14.** Distribution of stellar particles inside a sphere of 4 kpc radius located at 8 kpc from the centre of the remnant of a 5:1 merger between a satellite and a disk galaxy, after 4.5 Gyr of evolution. In all panels, the black dots represent particles from the satellite and grey dots particles from the disk. The top panel shows the distribution of particles in frequency space, whereas the bottom panels correspond to the apocentre vs. pericentre space (left), the  $E - L_z$  (middle) and the  $V_R - V_\phi$  (right) projections. Notice that streams are much better defined in frequency space than in any other projection.

is, we assign to each grid element  $N_p$  particles, where this number is drawn from a Poisson distribution with mean  $\langle N \rangle = (N_{\text{disk}} + N_{\text{sat}})/n_{\text{grid}}$ , i.e. equal to average number of stellar particles per grid element. We then compute the Fourier transform of this distribution and the corresponding 1-dimensional power spectra from the image. This procedure is repeated 1000 times, to yield an average power spectrum in each direction associated to a random distribution of particles in frequency space.

The results are shown in the bottom and middle panel of Fig. 15. The black solid line in each panel denotes the power spectrum obtained from the actual distribution of particles in frequency space. The blue solid line corresponds to the average power spectrum for our random distributions where the vertical error bars represent the rms dispersion around this average spectrum. As we can see, a statistically significant peak can be identified in the observed power spectrum along  $k_r$  (and also for  $k_\phi$ ). The wavenumber of this peak is

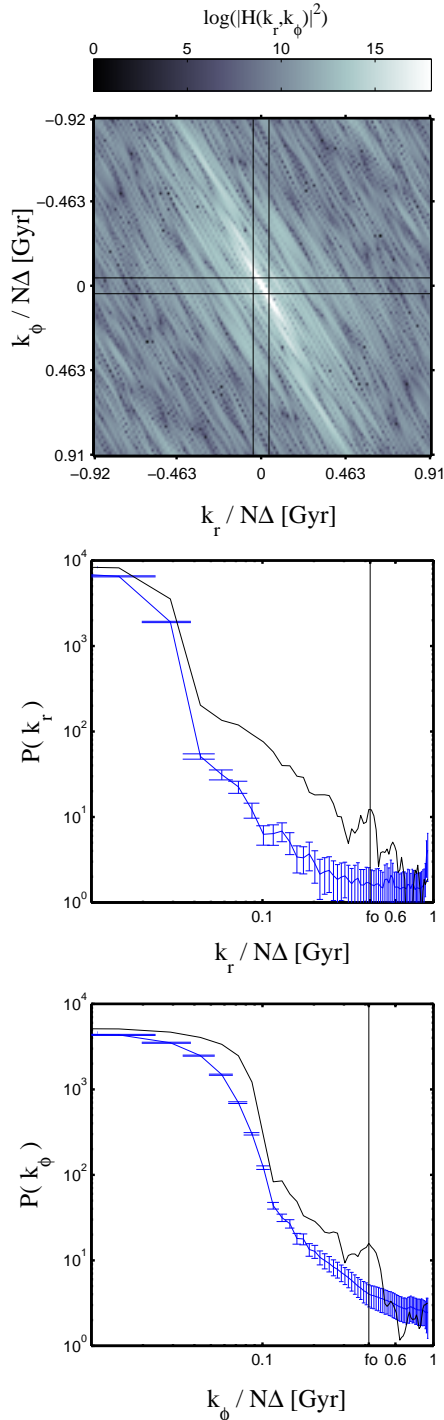


**Figure 15.** Top panel: Fourier transform of the distribution of particles in frequency space shown in the top panel of Fig. 14. As in Fig. 7 the middle and central panels depict the 1-d power spectra around  $k_\phi \sim 0$  and  $k_r \sim 0$ , respectively. The vertical lines in these panels show the location of the peak associated to the average separation between streams in frequency space, and can be used to estimate the accretion epoch. The blue curve corresponds to the average power spectrum obtained from a random distribution of particles in frequency space. The error bars represent the rms dispersion from this average spectrum.

$f_0 \approx 0.43$  Gyr for both the radial and angular directions. This corresponds to an estimated accretion time of 2.7 Gyr. Recall that this simulation is evolved for 4.5 Gyr. However, the satellite only starts to loose a significant amount of stars  $\sim 1$  Gyr after infall (see Figure 3 of VH08). Therefore, we may conclude that the time of disruption of a satellite can be reasonably estimated even in a simulation with a live host.

## 6 DISCUSSION AND CONCLUSIONS

We have studied the suitability of the space of orbital frequencies to identify debris from past accretion events. We analysed simulations of the disruption of a satellite galaxy in various scenarios. We have found that in frequency space, particles in a given volume of physical space are distributed in several lumps, each of them associated with a different stream.

For time-independent potentials, streams are distributed in a regular pattern along lines of constant frequency. As time goes by, the number of streams at a given physical location increases while the separation between adjacent streams decreases. This characteristic separation or scale can be used to estimate the time of accretion of the object through a Fourier analysis.

We have also addressed how the time evolution of the host affects substructure in frequency space. As an example, we have considered the case in which the mass of the host is increased exponentially in time on two different timescales. We find that in contrast with the actions which are adiabatic invariants for slowly varying potentials, the frequencies always evolve in time, closely following the rate of change of the host potential. This evolution however does not destroy the clumpiness present in frequency space. Streams still look lumpy and are regularly distributed in this space, even if the host potential varies on a very short timescale (when even the actions are no longer invariant). Interestingly in this case, streams are not exactly distributed along straight lines of constant frequency but rather on lines whose curvature depends on the timescale of growth of the potential. This implies that, contrary to previous claims (e.g. Peñarrubia et al. 2006; Warnick et al. 2008), the final distribution of streams does retain information on the evolution in time of the host.

Finally, we have analysed a full N-body simulation of the accretion of a satellite galaxy onto a disk galaxy. Due to the inclusion of other physical processes (such as self-gravity, dynamical friction and the variation in time of the distribution of mass in the system), the distribution of satellite particles in frequency space looks somewhat less regular than in the previously discussed idealised cases. Nevertheless, the space of frequencies is still rich in substructure associated to streams. Furthermore, even in this case Fourier analysis techniques can be used to estimate the time of accretion reasonably well, although in general, only a lower limit is obtained.

For all these examples we have compared the final distribution of streams in the most commonly used spaces to identify satellite debris. These comparisons have shown that frequency space contains information that is either not present or is not simply obtained in other spaces. In general streams are most sharply defined in frequency space.

One important simplification in our analysis is to con-



sider the accretion of a single satellite galaxy. In reality, the process of the formation of a galaxy like the Milky Way will have involved many mergers (in the range of 5 – 40, see De Lucia & Helmi 2008). Therefore it is possible, and even likely, that their debris will overlap in frequency space. However, as we have shown, the separation between adjacent streams in frequency space is predicted to be different for mergers that took place at different epochs. Moreover, the location of their debris in frequency space at the present time is dependent upon the initial orbital conditions. Consequently we expect the overlap to be incomplete and hence the identification of their remnants to be feasible. We are currently analysing the full cosmological high resolution N-body simulations of the Aquarius Project (Springel et al. 2008) in order to address this issue and to understand what to expect in the context of the hierarchical paradigm of structure formation.

#### ACKNOWLEDGEMENTS

We are very grateful to Alvaro Villalobos for providing the simulation used in Section 5 and Daniel Carpintero for the software for the spectral analysis used in Section 5.1. NWO is acknowledged for financial support through a VIDI grant to AH.

#### REFERENCES

- Arifyanto M.I., Fuchs B., 2006, *A&A*, 449, 533  
 Belokurov V., et al., 2006, *ApJ*, 642, L137  
 Binney J., Spergel D., 1984, *MNRAS*, 206, 159  
 Binney J., Tremaine S., 2008, *Galactic Dynamics*. Princeton Univ. Press, Princeton, NJ  
 Bullock J.S., Kravtsov A.V., Weinberg D.H., 2000, *ApJ*, 539, 517  
 Carpintero D.D., Aguilar L.A., 1998, *MNRAS*, 298, 1  
 De Lucia G., Helmi A., 2008, *MNRAS*, in press (arXiv:0804.2465)  
 Eggen O.J., 1996, *AJ*, 112, 1595  
 Font, A.S., Johnston, K.V., Bullock, J.S., Robertson, B.E. 2006, *ApJ*, 646, 886  
 Goldstein H., Poole C.P., Saffo J.L., 2001, *Classical Mechanics*. Addison-Wesley, Massachusetts  
 Gould A., 2003, *ApJ*, 592, L63  
 Gould A., Salim S., 2003, *ApJ*, 582, 1001  
 Governato F., et al., 2004, *ApJ*, 607, 688  
 Governato F., Willman B., Mayer L., Brooks A., Stinson G., Valenzuela O., Wadsley J., Quinn T., 2007, *MNRAS*, 374, 1479  
 Grillmair, C.J. 2006, *ApJ*, 645, L37  
 Helmi A., de Zeeuw P.T. 2000, *MNRAS*, 319, 657  
 Helmi, A., White, S.D.M. 1999, *MNRAS*, 307, 495  
 Helmi A., White S.D.M., de Zeeuw P.T., Zhao H., 1999, *Nat*, 402, 53  
 Helmi A., White S.D.M., Springel V., 2003, *MNRAS*, 339, 834  
 Helmi A., Navarro J.F., Nordström B., Holmberg J., Abadi M.G., Steinmetz M., 2006, *MNRAS*, 365, 1309  
 Hernquist L., 1990, *ApJ*, 356, 359  
 Ibata R.A., Gilmore G., Irwin M.J., 1994, *Nat*, 370, 194  
 Ibata, R., Irwin, M.J., Lewis, G.F., Ferguson, A.M.N., Tanvir, N. 2003, *MNRAS*, 340, L21  
 Klement R., Fuchs B., Rix H.-W., 2008, *ApJ*, 685, 261  
 Klypin A., Gottlöber S., Kravtsov A.V., Khokhlov A.M., 1999, *ApJ*, 516, 530  
 Knebe A., Gill S., Kawata D., Gibson B.K., 2005, *MNRAS*, 357, 35  
 McMillan P.J., Binney J., 2008, *MNRAS*, 390, 429  
 Miyamoto M., Nagai R., 1975, *PASJ*, 27, 533  
 Moore B., Ghigna S., Governato F., Lake G., Quinn T., Stadel J., Tozzi P., 1999, *ApJ*, 524, L19  
 Navarro J.F., Frenk C.S., White S.D.M., 1996, *ApJ*, 462, 563  
 Navarro J.F., Helmi A., Freeman K.C., 2004, *ApJL*, 601, L43  
 Peñarrubia J., Benson A.J., Martínez-Delgado D., Rix H.W., 2006, *ApJ*, 645, 240  
 Perryman M.A.C., et al. 2001, *A&A*, 369, 339  
 Plummer H.C. 1911, *MNRAS*, 71, 460  
 Salim S., Gould A., 2003, *ApJ*, 582, 1011  
 Scannapieco C., White S.D.M., Springel V., Tissera P.B., 2009, arXiv 0812.0976  
 Springel V., et al., 2008, *MNRAS*, 391, 1685  
 Steinmetz, M., Navarro, J.F. 1999, *ApJ*, 513, 555  
 Yanny B. et al., 2003, *ApJ*, 588, 824  
 Villalobos A., Helmi A., 2008, *MNRAS*, in press (arXiv:0803.2323)  
 Vogelsberger M., White S.D.M., Helmi A., Springel V., 2008, *MNRAS*, 385, 236  
 Warnick K., Knebe A., Power C., 2008, *MNRAS*, 385, 1859  
 Wells C.G., Siklos S.T.C., 2006, *Eur. J. Phys.* 28, 105  
 White S.D.M., Rees M.J., 1978, *MNRAS*, 183, 341  
 Zwitter T., et al., 2008, *AJ*, 136, 421